2014-12

In-depth understanding of the relation between CuAlO2 particle size and morphology for ozone gas sensor detection at a nanoscale level

ACS Applied Materials and Interfaces, Washington, DC : American Chemical Society - ACS, v. 6, n. 23, p. 21739-21749, Dec. 2014
http://www.producao.usp.br/handle/BDPI/50718

ACS APPLIED MATERIALS & INTERFACES

Research Article

www.acsami.org

In-Depth Understanding of the Relation between $CuAlO_2$ Particle Size and Morphology for Ozone Gas Sensor Detection at a Nanoscale Level

S. Thirumalairajan,* Valmor R. Mastelaro,* and Carlos A. Escanhoela, Jr.

Instituto de Física de São Carlos (IFSC), University de São Paulo, CP 369, 13560-970 São Carlos, SP, Brazil

Supporting Information

ABSTRACT: A morphology-dependent nanomaterial for energy and environment applications is one of the key challenges for materials science and technology. In this study, we investigate the effect of the particle size of $CuAlO_2$ nanostructures prepared through the facile and hydrothermal process to detect ozone gas. Phase analysis and structural information were obtained using X-ray diffraction and micro-Raman studies. The chemical states of $CuAlO_2$ atomic species were determined by X-ray photoelectron spectroscopy. Electron microscopy images revealed the flower and hexagonal shape constituted of pentagon and oval $CuAlO_2$ nanoparticles with average size ~40 and 80 nm. The specific surface area was measured and found to be 59.8 and 70.8 $m^2 g^{-1}$, respectively. The developed $CuAlO_2$ nanostructures not only possess unique morphology but also influence the ozone gas sensing performance. Among the two structures, $CuAlO_2$, with hexagonal morphology, exhibited superior ozone detection for 200 ppb at 250 °C, with a response and good recovery time of 25 and 39 s compared to the flower morphology (28 and 69 s). These results show that not only does the morphology play an major role but also the particle size, surface area, gas adsorption/desorption, and grain−grain contact, as proposed in the gas sensing mechanism. Finally, we consider $CuAlO_2$ material as a good candidate for environment monitoring applications.

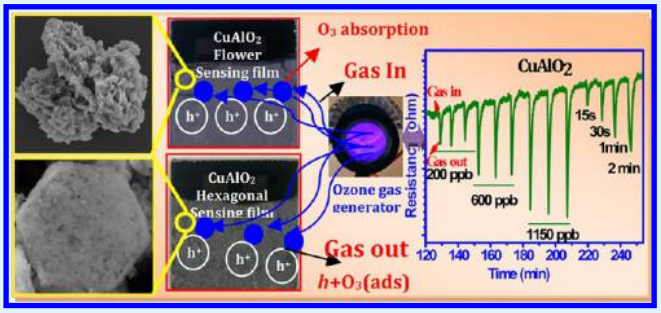

KEYWORDS: *$CuAlO_2$, hexagonal, flowers, morphology, nanoparticles, ozone gas*

1. INTRODUCTION

Gas detection for safety purposes, health, and security by metal oxide semiconductor sensors has attracted great attention because of it technological and fundamental scientific importance.[1] This has been considered promising due to its unique advantages, such as high sensitivity, stability, and short response time, all of which are considered essential features for optimized sensors. It is extremely sensitive to cost-effective detection of toxic gas molecules and is the main driver for the development of new chemical sensors.[2] Regarding gas sensing applications, an ongoing technological challenge concerns the selective detection of toxic and flammable analytes such as CO, NO_2, H_2, CO_2, and O_3, whose monitoring is important for safety reasons.[3−7] Ozone (O_3) is a powerful oxidizing reagent and a very strong disinfectant whose appearance in the atmosphere is very harmful for human health.[8] As per the World Health Organization (WHO), the air quality guidelines for ozone exposure of 1 ppm cause burning eyes, headaches, and irritation to the respiratory passages. An individual, if exposed to 0.2 ppm or 200 ppb of O_3 for 2 h, will sustain a loss of 20% in breathing capacity and, if exposed to 1 ppm of O_3 for 6 h, will suffer an attack of bronchitis. It was observed that a mouse exposed to 10 ppm of O_3 did not survive.[9−12] However, during the past decade, most studies have been focused on n-type semiconductor oxides such as ZnO, WO_3, Fe_2O_3, SnO_2, etc., for toxic gas sensing applications operating at a relatively high working temperature around 300 °C.[13−16] The gas sensing characteristics of p-type materials have been rarely investigated, although the architectures combined with n-type ones have been reported.[17−19] Recently, research is focused on p-type semiconductor materials, particularly transparent conducting oxide (TCO) materials for toxic gas sensing applications. However, the gas sensing properties of such pristine Cu based TCO materials are rarely explored and the mechanism still remains unclear.

TCO p-type materials of Cu-based delafossite compounds have been recently investigated because they possess mutually exclusive properties of low electrical resistivity and high optical transparency in the visible range.[20] Delafossite oxides are a class of materials with the ABO_2 chemical structure, where A is a monovalent ion such as Cu^{1+} or Ag^{1+} and B is a trivalent ion such as Al^{3+}, Cr^{3+}, or Ga^{3+}. These oxides crystallize in the 3R rhombohedral (space group *R*3*m*) or the isomorphic 2H hexagonal (space group *P*63/*mmc*) structures.[21] Usually,

Received: October 16, 2014
Accepted: November 17, 2014
Published: November 17, 2014

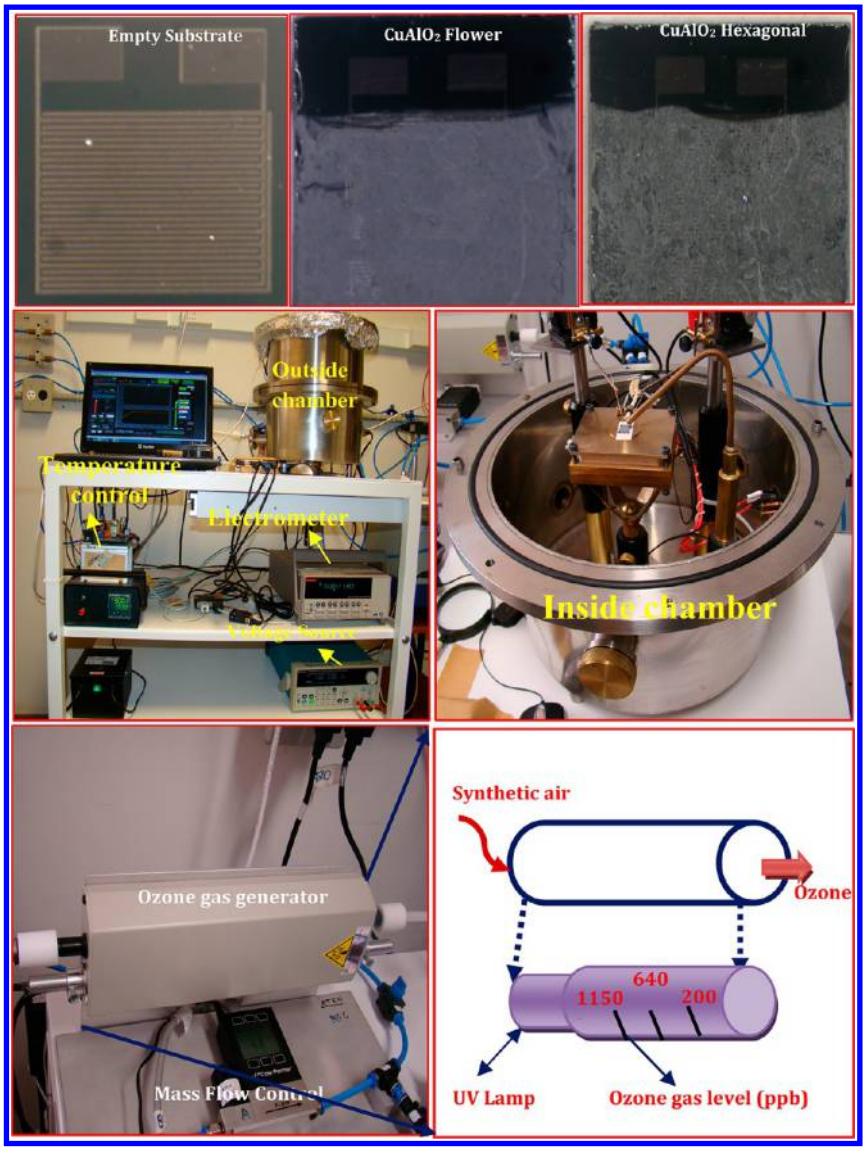

Figure 1. Photograph of sensing films and ozone gas measurement setup.

$CuAlO_2$ is thermodynamically unstable below 1000 °C in air and easily decomposes to the Cu^{2+} compounds such as CuO and $CuAl_2O_4$ under these conditions.[22] Under wet chemical conditions, the reduction in energy consumption for synthesizing $CuAlO_2$ can be attributed to a highly efficient absorption of energy and the coupling efficiency of metal nitrate and surfactant, and also many inorganic materials are able to strongly couple after calcination at 1100 °C.[23]

It is well-known that gas sensing applications of nanostructured materials are directly related to the target gas adsorption−desorption, particle size, shape, surface area, grain to grain contact, and synthesis methods.[24−28] Various physical and chemical methods are available to prepare $CuAlO_2$ materials,[29−32] but synthesis strategies to tailor the surface properties of nanostructures and to systematically unravel the shape-guiding process and the growth mechanism responsible for their enhanced functionalities still remain a challenge.[33] The surfactant-assisted self-assembly hydrothermal method is one of the most excellent processes to form different morphologies with a porous surface, because this demands a comprehensive understanding of various operating parameters, such as reaction and calcination temperature along with the reaction time. Recently, the morphology and size-dependent properties of semiconductor oxides have triggered intensive attention in materials science research, owing to their crucial role in significant applications.[34] However, to the best of our knowledge, morphology-dependent ozone gas sensor activities of $CuAlO_2$ nanostructures have not been explored in the open literature.

Herein, for the first time, we report single phase $CuAlO_2$ nanostructured materials prepared by a cost-effective surfactant-assisted hydrothermal method with different morphologies, such as hexagonal and flower structures. It is worth noting that ozone gas sensor devices are assembled using p-type $CuAlO_2$ nanostructures, enabling more systematic assessment of sensor response. An understanding of the influence of shape, size, and grain to grain contact and how the width of the charge accumulation layer affects ozone gas detection are all helpful for understanding the impact on gas-sensing performance and gas sensing mechanism.

2. EXPERIMENTAL SECTION

Materials synthesis. $CuAlO_2$ nanostructures were synthesized by the surfactant-assisted hydrothermal process. All chemicals purchased

were analytical pure grade and used without further purification. In the experimental process, $Cu(NO_3)_2{\cdot}3H_2O$ and $Al(NO_3)_2{\cdot}9H_2O$ were used as precursor, and citric acid and hexadecyltrimethylammonium bromide (CTAB) were used as surfactant. Two different experiments were employed for the synthesis of $CuAlO_2$. In the first experiment, an equal molar amount of the starting materials, i.e. $Cu(NO_3)_2{\cdot}3H_2O$, $Al(NO_3)_2{\cdot}9H_2O$, and surfactant citric acid were dissolved in 90 mL of double distilled water with magnetic stirring, followed by the addition of 5 mL of EG and 2 g of NaOH as a mineralizar to form a light blue colored solution. In the second experiment, citric acid was replaced by CTAB in the first experiment and added to the starting material, resulting in a transparent blue colored solution. The total molar amount of metal nitrates was equal to the molar amount of surfactant in the solution. The two solutions prepared were transferred separately into a 110 mL Teflon-lined stainless steel autoclave, sealed, and maintained at 200 °C for 12 h. The autoclave was cooled down to room temperature naturally. The obtained products were separated by centrifugation, washed with deionized water and anhydrous ethanol several times, and then dried in air at 80 °C for 10 h. Finally, the powder was annealed at 1100 °C for 5 h to obtain $CuAlO_2$ samples with high crystallinity and used for further characterization.

Materials characterization. The surface morphology and particle size of the prepared nanostructures were characterized using scanning electron microscopy (F50 INSPECT) and transmission electron microscopy (TECNAI F20) at an accelerated voltage of 200 kV. The phase, purity, and crystallite size of the prepared nanostructures were determined using X-ray diffraction (XRD) Cu Kα1 radiation (K = 1.5406 Å, Rigaku diffractometer, model DMax-2500 PC) in the 2θ range from 10 to 80 °C with a step of 0.02° at a scanning speed of 2°/min, maintained at an operating voltage and current of 40 kV and 40 mA. The Raman spectrum was obtained for the prepared samples placed on a glass wafer using a LabRAM HR800 Raman microscope with a 514 nm Ar-ion laser (10 mW). X-ray photoelectron spectroscopic measurement was carried out in an Thermo K-Alpha XPS (Thermo Scientific, Inc.) using a dual anode source, and the measurement was carried out using Al Kα (1486.6 eV). The Brunauer–Emmett–Teller (BET) surface area was analyzed using a Micromeritics ASAP 2020 nitrogen adsorption–desorption apparatus.

Fabrication of sensing films and ozone gas measurement. The morphologically different $CuAlO_2$ nanostructure powders (10 mg) were dispersed in 1 mL of isopropyl alcohol by an ultrasonic cleaner for 30 min, and the suspension was dropped onto a Si/SiO_2 substrate containing 100 nm thick Pt electrodes separated by a distance of 50 μm. The thickness of the film was controlled to 800 nm for both the morphologies. The substrates were then heated to 90 °C for 10 min to evaporate the solvent, followed by calcination at 500 °C for 2 h in an electric furnace in air, to stabilize the sample before the gas sensing measurements were performed, as shown in Figure 1.

The sensor sample was inserted into a test chamber at controlled temperature under different low ozone concentrations of 200, 600, and 1150 ppb. The ozone gas was formed by the oxidation of oxygen molecules of dry air (8.3 cm^3/s) with a calibrated pen-ray UV lamp (UVP, model P/N 90-0004-01). The electrical resistance was measured using a Keithley (model 6514) electrometer at an applied dc voltage of 1 V. The dry air containing ozone was blown directly onto the sensor placed on a heated holder as shown in Figure 1.

The sensing response (S), defined as $S = R_{air}/R_{gas}$, is the electric resistance of the sensor exposed to the resistance in the air (R_{air}) and to the target oxidizing gas (R_{gas}). The response time of the sensor was defined as the time required for a change in the electrical resistance to reach 90% of the initial value when exposed to ozone gas. Similarly, the time required for the electrical resistance of the sensor to reach 90% of the initial value after the ozone gas has been turned off is the recovery time. During the measurements the humidity was under controlled conditions within the range 50–60% RH.

3. RESULTS AND DISCUSSION

Morphology and particle size analysis. The surface morphology of two kinds of $CuAlO_2$ structures was observed from SEM images. The lower magnification (5000×) image in Figure 2a indicates that the flower structure consists of $CuAlO_2$ nanoparticles synthesized by a hydrothermal process using citric acid as surfactant. The diameter of the microflower is ~3 μm. A detailed view of the individual $CuAlO_2$ flower can be observed from the higher magnification (20000×) image (Figure 2b), which clearly shows that the $CuAlO_2$ flowers consist of many pentagon nanoparticles of average size ~80 nm. These nanoparticles emerge from the single center, thereby acquiring the formation of a flower structure via a self-assembly process. Further, when CTAB was used as a surfactant, the hexagonal shaped $CuAlO_2$ structure was obtained. The low-magnification image (Figure 2c) clearly reveals that the shape of the as prepared structure is a hexagonal plate. The high-magnification image (Figure 2d) demonstrates that the individual hexagonal shape has diameter ~2 μm and thickness 100 nm (from the vertical view of the inset in Figure 2d) and it is comprised of oval shape nanoparticles in the range ~40 nm. A clear grain boundary can be observed on the surface of $CuAlO_2$ flowers and hexagonal plates, indicating they are formed by the oriented aggregation of small $CuAlO_2$ nanoparticles.

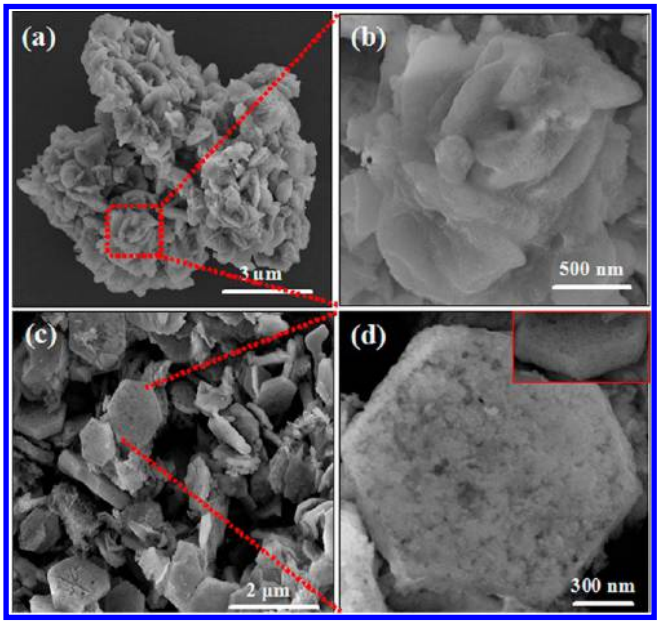

Figure 2. SEM image of the different $CuAlO_2$ nanostructures: (a) low magnification and (b) high magnification of flower structure; (c) low and (d) high magnification of hexagonal structure (insert) vertical view.

It is understood that for the formation of different $CuAlO_2$ morphologies with controlled size, OH^- ions originating from citric acid and CTAB play a major role. When citric acid was used as surfactant, the OH^- ions absorbed on the surface of the $CuAlO_2$ particles directed the self-assembly process of the nanoparticles by molecular interaction to form the flower structure with certain crystallographic orientations.[35] When CTAB takes the role of surfactant, OH^- ions absorb on the surface of $CuAlO_2$ particles formed in the initial stage of the reaction process, which decreases the surface energy of the particles in a particular undisturbed direction, and further growth takes place by means of particle attachment of $CuAlO_2$ nanoparticles.[36] The process continues until plates of hexagonal structure were obtained. The surfactant not only provides

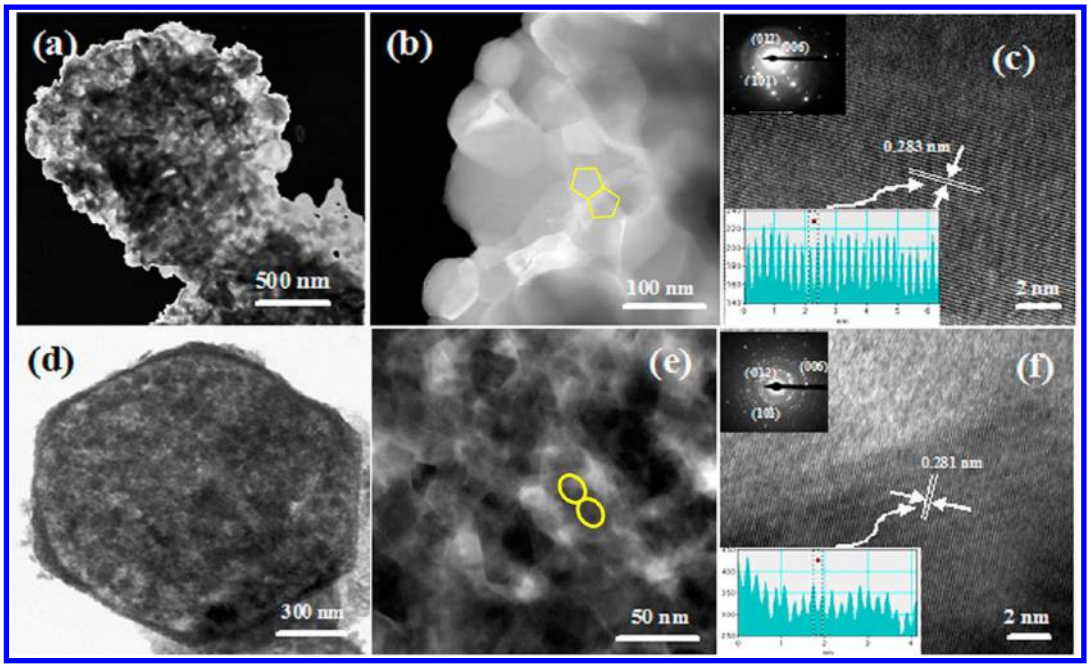

Figure 3. (a and d) Low magnification and (b and e) high magnification TEM (inset cartoon shape of particle); (c and f) HRTEM image of different $CuAlO_2$ morphologies—flower and hexagonal nanostructure; (inset top) corresponding SAED pattern; (inset bottom) corresponding lattice interplanar spacing.

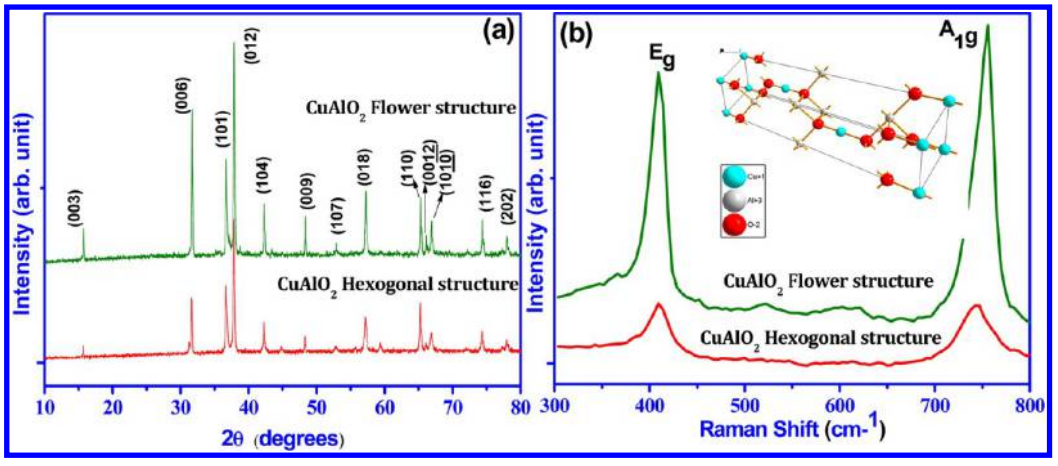

Figure 4. (a) XRD pattern; (b) Raman spectra of different $CuAlO_2$ nanostructures (inset—crystal structure image).

constructive sites for the growth of particle assemblies but also influences the formation process, including aggregation, nucleation, growth, flocculation, and coagulation. The surfactant was found to have a specific mechanism involved in the synthesis of nanostructures; that is, during the synthesis process, the surfactants were absorbed by the growing crystal and depending upon the precursor concentration and surfactant property, they moderate the growth rate of crystal faces, which thereby controls the shape and size through an Ostwald ripening process.[37] It was observed that the flower and hexagonal morphologies of $CuAlO_2$ structures could be reproduced using the surfactant-assisted hydrothermal process used in the present study. Further, $CuAlO_2$ samples without surfactant were also prepared, where only agglomerated structures were observed (Figure S1, Supporting Information), which is of no interest for the present study.

In order to further research inside the morphology of $CuAlO_2$ flowers and hexagonal structure, typical TEM and HRTEM images were collected as shown in Figure 3. The low magnification TEM image of the $CuAlO_2$ flowers shown in Figure 3a reveals the structure has diameter ~3 μm. A part of a flower has been further magnified in Figure 3b, to show the flower constituted of numerous $CuAlO_2$ pentagon nanoparticles with average size ~80 nm, which is in good agreement with those shown in Figure 2b.

Figure 3d presents the typical TEM image of the formed uniform hexagonal plate structure with average size ~2 μm, which is composed of radically assembled oval nanoparticles of size ~40 nm (Figure 3e). When closely observed, it can be concluded that the interconnections and packing of $CuAlO_2$ nanoparticles are responsible for the flower and hexagonal structure formation. The HRTEM image recorded at the tip of the individual $CuAlO_2$ flowers and hexagonal nanostructure is shown in Figure 3c and f. It was observed that particles have the same crystallographic orientation, like a single crystal. In addition, the interfringe distance was measured to be 0.283 and

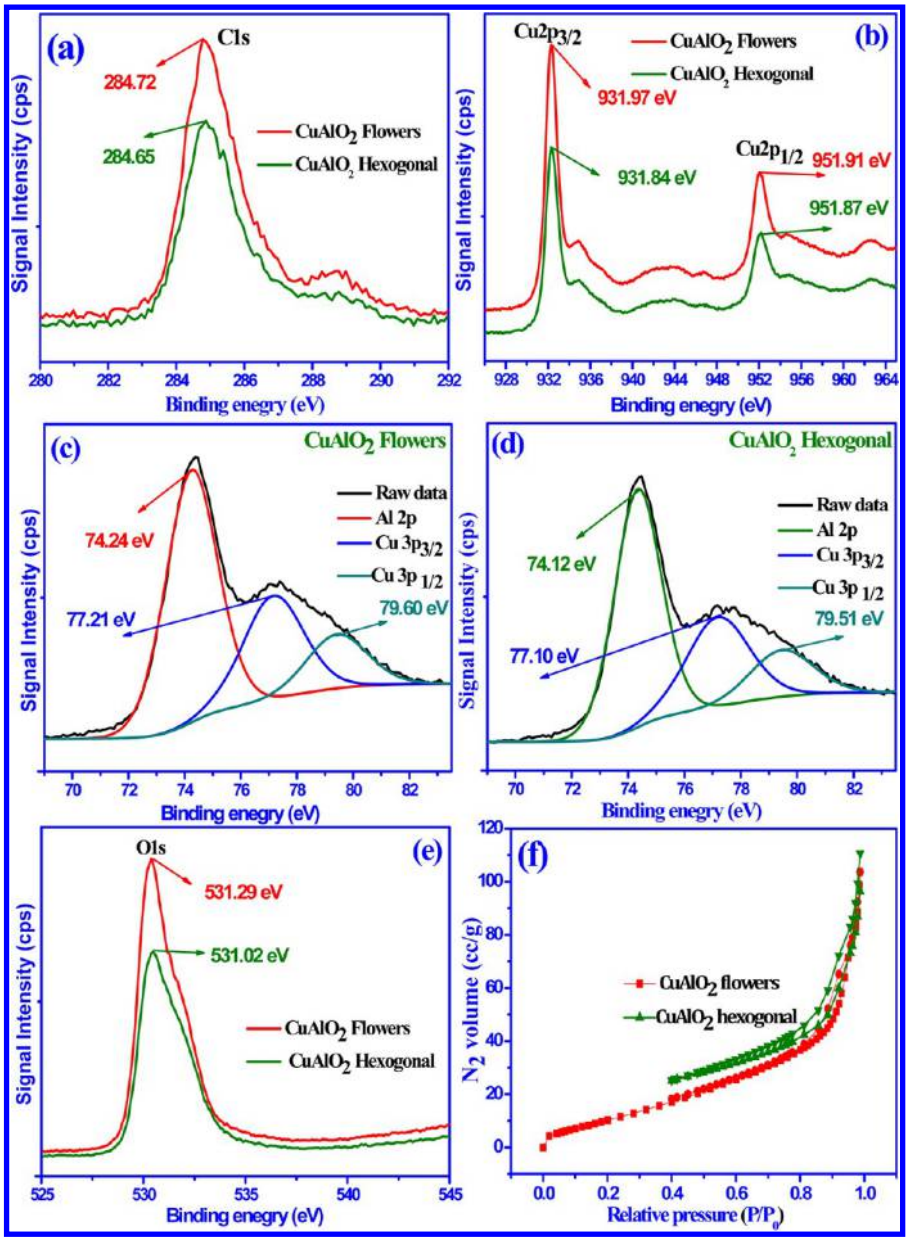

Figure 5. XPS spectra of morphologically different $CuAlO_2$ nanostructures: (a) C 1s line after offset; (b) local fine scanning of Cu; (c) $CuAlO_2$ flower; (d) $CuAlO_2$ hexagonal local fine scanning of A1 2p and Cu 3p after fitting; (e) local fine scanning of O 1s; (f) nitrogen adsorption–desorption isotherms.

0.281 nm based on the measurements of randomly selected 50 fringes, as evident in Figure (2c and f inset bottom). The corresponding lattice interplanar spacing is the lattice plane (012), and in the same direction further growth of the structure takes place. At the top right corner (inset) of Figure 3c and f, the SAED pattern of the two nanostructures has been presented. The bright diffraction spots can be indexed to the rhombohedral structure of $CuAlO_2$ with single crystalline nature. The major diffraction spots corresponds to (012), (006), and (101) planes. No diffraction spots were attributed to the secondary or impurity phases. Thus, by correlating the outcome from TEM and HRTEM images, it can be concluded that the observed results are in good agreement with SEM analysis.

Structural analysis. The X-ray diffraction patterns shown in Figure 4a were used to determine the phase, purity, crystallite size, and structure of the prepared $CuAlO_2$ nanostructures. The sharp and narrow diffraction peaks suggest the good crystallinity of both the samples with hexagonal and flower shaped morphology. All the diffraction peaks are indexed to the single phase of $CuAlO_2$. The structural model adopted is a rhombohedral crystal system ($a = b = 2.8584$ Å, $c = 16.9580$ Å, within a maximum experimental error of ± 0.0003, $\alpha = \beta = 90°$, $\gamma = 120°$) with delafossite structure with $R\bar{3}m$ space group.[38] No other crystalline phases and other peaks related to impurity phases were detected in the XRD pattern, indicating that the $CuAlO_2$ samples of high purity could be obtained under synthetic conditions. The average crystallite size was estimated after correcting the instrumental contribution to the line broadening by the Debye–Scherrer formula[39] and was found to be ~85 and 50 nm for flowers and a hexagonal structure consisting of $CuAlO_2$ nanoparticles. The HRTEM image of the flowers and hexagonal structure discussed in the morphological analysis section shows clear lattice fringes along

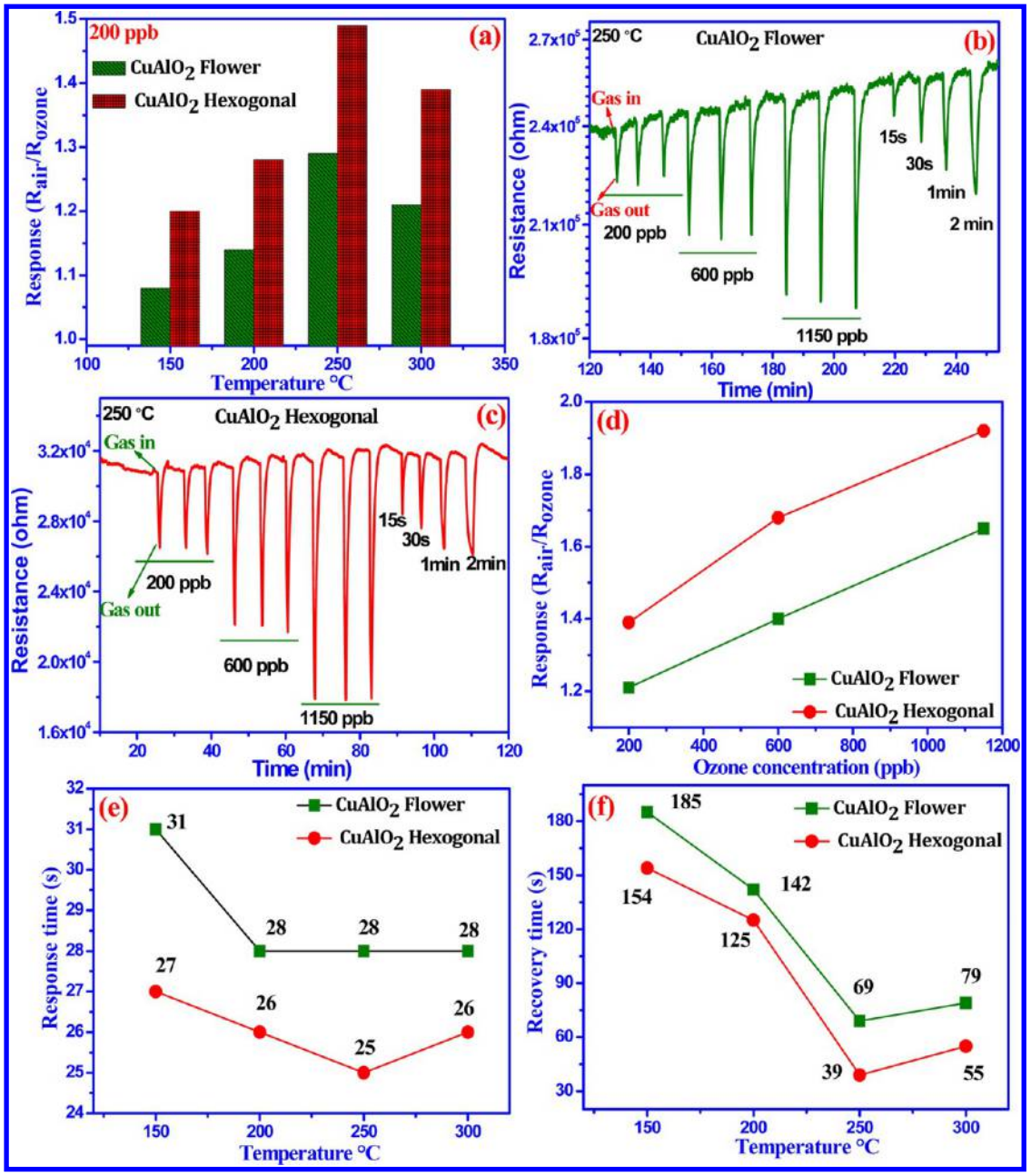

Figure 6. (a) Response to 200 ppb ozone (O_3) gas by the $CuAlO_2$ nanostructure working at different temperatures. (b and c) Transient sensing response of flowers and hexagonal structure for different concentrations and times of O_3 gas at 250 °C. (d) Sensing response as a function of ozone concentration. (e) Response time (s) and (f) recovery time (s) of the statistical reports of different $CuAlO_2$ nanostructures.

the growth direction. The spacing of the lattice fringes was 0.283 and 0.281 nm, which can be well indexed with the "*d*" spacing of the (021) of the $CuAlO_2$ rhombohedral structure, and the lattice parameters are almost the same for the flowers and hexagonal morphology. Specially, by comparison, the diffraction peak intensities of the hexgonal product are stronger than those of the flower morphology. Further, in the Cu-based delafossite structure ($CuAl^{3+}O_2$), each Cu atom is linearly coordinated between two oxygen atoms, constructing O−Cu−O dumbbells parallel to the *c* axis, where they proposed an alternative stacking of Cu^1 and layers of nominal AlO_2 composition consisting of AlO_6 octahedra sharing edges[40] as shown in Figure 4b (inset).

In addition, the prepared single phase $CuAlO_2$ samples were probed using Raman spectroscopy to detect the presence of lattice defects in solids. Figure 4b presents the typical room temperature Raman spectra of the $CuAlO_2$ nanostructures for the 200−1000 cm^{-1} region. Group theory analysis demonstrated that a primitive cell of delafossite compound has four atoms with space group $R\bar{3}m$, and there are 12 optical phonon modes (A_{1g}, E_g, $3A_{2u}$+, $3E_u$) at the center of the Brillouin zone (BZ).[41] In the present $CuAlO_2$ flowers and hexagonal structure, the A_{1g} and degenerate E_g symmetries are Raman active modes that correspond to 409 and 415 cm^{-1} and 755 and 765 cm^{-1} within a maximum experimental error of ±0.01, as also reported for single crystals of $CuAlO_2$.[42] The A_{1g} mode corresponds to the vibration of the Cu−O bond along the *c*-axis, while E_g represents the vibration in the plane perpendicular to the *c*-axis. The peak positions are in good agreement with the values reported for $CuAlO_2$.[42] These results

confirm that the prepared nanostructures are of a single phase and the peaks corresponding to other phases were not detected, indicating high purity of the prepared samples. The result also agrees with the results discussed in the XRD section.

To further identify the chemical composition and elements present in the prepared flowers and hexagonal structure of $CuAlO_2$ comprised of nanoparticles, X-ray photoelectron spectroscopy (XPS) measurements were carried out and the results are presented in Figure 5a−e. The carbon signal originates from the XPS measurement system. The survey spectra for different $CuAlO_2$ nanostructures indicate that adventitious C 1s, Cu 2p and 3p, Al 2p, and O 1s related core levels are detectable at an experimental error of ±0.02%. In Figure 5a, the C 1s peaks at 284.72 and 284.65 eV for flowers and hexagonal structure were used as an internal standard, and the other spectra are calibrated with the C 1s peak to correct the binding energy position. The binding energies of the Cu 2p3/2 and Cu 2p1/2 are found at 931.97 and 951.91 eV for $CuAlO_2$ flowers and at 931.84 and 951.87 eV for the $CuAlO_2$ hexagonal structure, respectively, as shown in Figure 5b. The measured Cu 2p3/2 and Cu 2p1/2 peaks were about 2 eV below 955 and 933.8 eV (the binding energy of the Cu^{2+} in CuO).[43] The obtained binding energies are less than for the Cu +2 state; this confirms that Cu in $CuAlO_2$ is in the +1 state. This confirms that, in the present samples, the impurity phases of CuO and $CuAl_2O_4$ are eliminated due to annealing treatment.[44]

From Figure 5c and d, it is observed that there exists Al 2p peak of Al^{3+} (around 74.24 and 74.14 eV for flower and hexagonal structure) and a Cu 3p3/2 peak (around 77.21 and 77.10 eV) and a Cu 3p1/2 (79.60 and 77.51 eV) peak of Cu+ in the prepared nanostructures after fitting. Element Al has nearly equal binding energies in Al_2O_3, $CuAl_2O_4$, and $CuAlO_2$ around 73.7−74.4 eV.[45] But in the case of Al 2p states, the binding energy was found to have lesser value than its corresponding simple oxide. This may be due to interaction between Cu 3p and Al 2p. It is expected that Al element could be in the form of $CuAlO_2$. The O 1s peak located at 531.29 and 531.09 eV for flowers and the hexagonal structure reveals the presence of chemisorbed O-containing species, ascribed to the lattice oxygen of the $CuAlO_2$, as shown in Figure 5e. All the binding energies of Cu, Al, and O values indicate that the elements are in a chemically bonded state. Further confirmation of the chemical composition was also carried out using EDAX analysis (Figure S2, Supporting Information). The atomic ratio of Cu/Al was evaluated and found to be 1.089 for $CuAlO_2$ flowers and hexagonal structures. Composition analyses along with structural results indicate that the phase of the prepared flower and hexagonal morphology exists as $CuAlO_2$.

The surface area of a material is an important parameter which is responsible for achieving good sensing performance.[46] The surface area of $CuAlO_2$ flower and hexagonal structures was measured via the BET method using nitrogen adsorption and desorption measurement, shown in Figure 5f. The hysteresis loop in the high-pressure range ($0.8 < P/P_0 < 1$) can probably be associated with larger pores that could be formed between the aggregation of secondary particles of the prepared $CuAlO_2$ nanostructures. From the shape of the hysteresis loop, they were found to be of H3 type, which is again characterized for slit shape pores. The BET specific surface areas of $CuAlO_2$ flowers and hexagonal structures were calculated to be 59.8 and 70.8 $m^2\ g^{-1}$, respectively. The results suggest that the surface area distribution of the $CuAlO_2$ hexagonal structure is larger than that of flowers, due to its dimension formed by the aggregation of the $CuAlO_2$ nanoparticles, and hence could show good sensing behavior.

Ozone gas sensing measurment and mechanism of p-type $CuAlO_2$ nanostructures. The semiconductor oxide sensor response is highly influenced by parameters such as operating temperature and gas concentration.[47] The comparison of gas sensor response for the same material with different morphologies can best be accomplished, if the response of the ensemble of sensors can be measured simultaneously under identical experimental conditions. The fabricated sensor of $CuAlO_2$ with different morphologies was exposed to ozone vapor at various temperatures between 150 and 300 °C at intervals of 50 °C to find the optimum operating temperature of the ozone sensor at an experimental error of ±0.01%. Figure 6a indicates that the sensing response of the two $CuAlO_2$ nanostructures sharply increased with increasing working temperature at 250 °C for 200 ppb ozone gas in dry air. But, the sensor response is decreased at a working temperature of 300 °C. The reason behind the variation in sensor response put forward by the $CuAlO_2$ samples is the absorption of ozone gas at different optimum operating temperatures. At lower operating temperature, $CuAlO_2$ sensors display low response, which is decreased as the operating temperature increases due to the thermal excitation of electrons. At operating temperature 250 °C, high sensing response is evident, as the chemisorption process starts competing with the thermal excitation of electrons at this stage. This competition continues until the complete coverage of the $CuAlO_2$ surface with chemisorbed oxygen species. Beyond this temperature, the sensitivity starts to decrease due to the effect of the dominant thermal excitation of electrons and the saturation of oxygen adsorption on the resistance of the $CuAlO_2$ surface. Hence, high response to ozone gas exhibited at 250 °C was chosen for subsequent studies. In the case of hexagonal $CuAlO_2$ samples, the response was noticeably higher with respect to $CuAlO_2$ flowers at all temperatures, which can be associated with their particle size, morphology, surface area, and grain to grain contact.

Figure 6b and c shows the real-time response curve and the sensing responses of the two fabricated $CuAlO_2$ sensors upon exposure to different concentrations of ozone gas at various gas flow times and at the working temperature 250 °C, respectively. The resistance of the p-type oxide semiconductor ($CuAlO_2$) is known to decrease upon exposure to oxidizing gas (O_3).

The behavior of the sensitivity as a function of the operating temperature is usually explained with regard to the kinetics and mechanics of gas adsorption and desorption on the surface of semiconductor materials.[48] Furthermore, reversibility and stability are the important factors that must be considered acceptable to be utilized for reliable applications. We could observe that the sensor also had a good reversibility and stability after three cycles of ozone gas on and off for all concentrations (200, 600, and 1150 ppb) at different gas exposure (15 and 30 s, 1 and 2 min) times. According to the above results, we could observe that both the $CuAlO_2$ nanostructures had a good response to ozone at 200 ppb. But the responses of hexogonal $CuAlO_2$ nanostructures toward ozone gas are much higher than those of the flower $CuAlO_2$ nanostructures. The gas response not only depends on the particle size but also depends on surface morphology, as the chemiresistive variation of the $CuAlO_2$ semiconductor is the result of the interaction between an analyte gas and the sample surface. Figure 6d reveals the gas response of the two gas

sensors as a function of the concentration of ozone at 250 °C. The results indicate that the gas response increased with an increase in ozone concentration. At a low concentration of 200 ppb of ozone, the sensitivity is about 1.1 and 1.4 for flowers and the hexagonal $CuAlO_2$ nanostructure, respectively. With increasing ozone concentration, the response of the sensor also sharply increased from 1.39 and 1.5 for flowers and from 1.71 to 1.92 with an experimental error of ±0.01% for the hexagonal structure at ozone concentrations of 600 and 1150 ppb. When the concentration is too low, the chemical activation of sensors is consequently small, leading to a small response. When the ozone concentration is increased beyond a threshold value, adsorbed gas molecules attract the charge transfer due to their enhanced activation.

The response and recovery time are other important parameters for toxic gas sensor application. Figure 6e and f shows the temperature-dependent response and recovery time of flowers and hexagonal $CuAlO_2$ nanostructures. From the results, it can be clearly found that the response and recovery time present similar tendencies with variation in temperature with an experimental error of ±0.01%. At lower temperature (150 °C), the response was 31 and 27 s with high recovery time (185 and 154 s) for flowers and hexagonal $CuAlO_2$ nanostructures, while at higher temperature (250 °C) the response was found to be 28 and 25 s with shorter recovery time of 69 and 39 s. It is noteworthy that the response and recovery time show a decreasing trend with an increase in operating temperature. These results can be explained as follows: at lower temperature, the number of ozone molecules interacting with the surface of $CuAlO_2$ is not sufficient, leading to longer response and recovery times. At higher temperature, more ozone molecules interact with the oxygen ions and decrease the response and recovery time. Furthermore, the fast response and recovery behavior was observed at 250 °C, which indicates the chemisorbed oxygen bonding on the $CuAlO_2$ nanocrystallites is strong due to low concentration (200 ppb). The adsorbed molecules take a shorter time to desorb, leading to a decrease in the recovery time with increase in temperature. On the other hand, the recovery time of $CuAlO_2$ sensing samples is shorter than other reported n-type sensors such as WO_3, SnO_2, and In_2O_3 etc.[13−16] Thus, from the above results we confirm that the response of the two fabricated $CuAlO_2$ sensors toward ozone gas strongly depends on the operating temperature as well as the concentration of test gas. The sensor temperature also regulates the activation energies of adsorption−desorption and thereby the kinetics of the surface chemisorption reaction, which is reflected in the response and recovery time of the sensor signal.[49] The results clearly demonstrate the great advantage of employing the $CuAlO_2$ hexagonal nanostructure for real-time monitoring of the ozone gas sensor for 200 ppb at 250 °C. It could be noticed from the SEM images (Figure S3, Supporting Information) that there was no change in surface morphology of both the $CuAlO_2$ nanostructures taken after gas sensing measurements. There was also no change in the composition of the sample after gas detection, which was confirmed from the XRD pattern (Figure S4, Supporting Information)

In general, the semiconductor gas sensor works on the basis of resistance (or conductivity) changes of the sensing materials caused by the adsorption and desorption reactions of oxidation/reduction gas molecules on the surface of the sensing film.[50]

In the present case, for $CuAlO_2$ p-type material, holes are the majority carriers. The acceptor level lies near the valence band, and at operating temperature, all the acceptor levels are ionized (filled), leaving holes in the valence band. The $CuAlO_2$ ion vacancies are the acceptors in this case, as shown in Figure 7

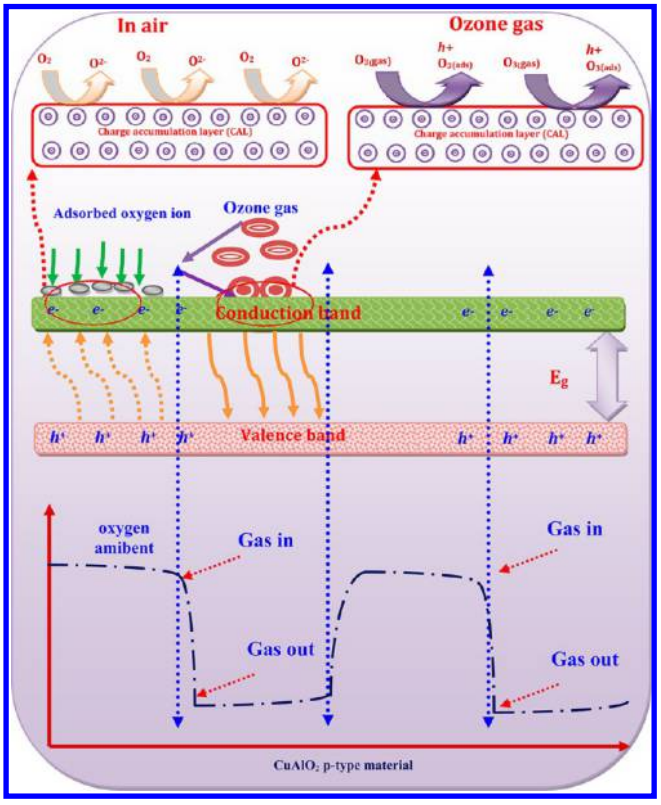

Figure 7. Schematic diagram for the change in sensor resistance upon exposure to air and oxidation gas (ozone) in the case of a p-type $CuAlO_2$ sensor.

(left side). As the $CuAlO_2$ surface is exposed to air, the oxygen molecules from the air get adsorbed on the surface of $CuAlO_2$ to form O_2^-, O^-, and O^{2-} ions by trapping electrons from the conduction band (eq 1); that is, the adsorption of negatively charged oxygen can generate holes. The same has been represented in the following equation.

$$O_2(\text{gas}) \Leftrightarrow O_2(\text{ads}) + h^+ \Leftrightarrow O_2^-(\text{ads}) + h^+ \Leftrightarrow 2O^-(\text{ads}) + h^+ \Leftrightarrow O^{2-}(\text{ads}) + h^+ \quad (1)$$

When oxidation gas ozone (O_3) is introduced to the surface of $CuAlO_2$ samples, the ozone molecules adsorb on the $CuAlO_2$ surface acting as acceptors. This surface trapping of lone-pair electrons causes band bending, which results in the formation of free holes and an increase in hole concentration near the interface forming the hole accumulated layer at the $CuAlO_2$ surface, which decreases the resistance of $CuAlO_2$ samples as shown in Figure 6 (right side). The following reaction (eq 2) takes place on the surface of the $CuAlO_2$ sensing film.

$$CuAlO_2 + O_3(\text{gas}) \Leftrightarrow CuAlO_2^+ - O_3^-(\text{ads}) \Leftrightarrow CuAlO_2 - O_3(\text{ads}) + h \quad (2)$$

The gas response in p-type oxide semiconductors is dependent on the morphology and particle size; this point of

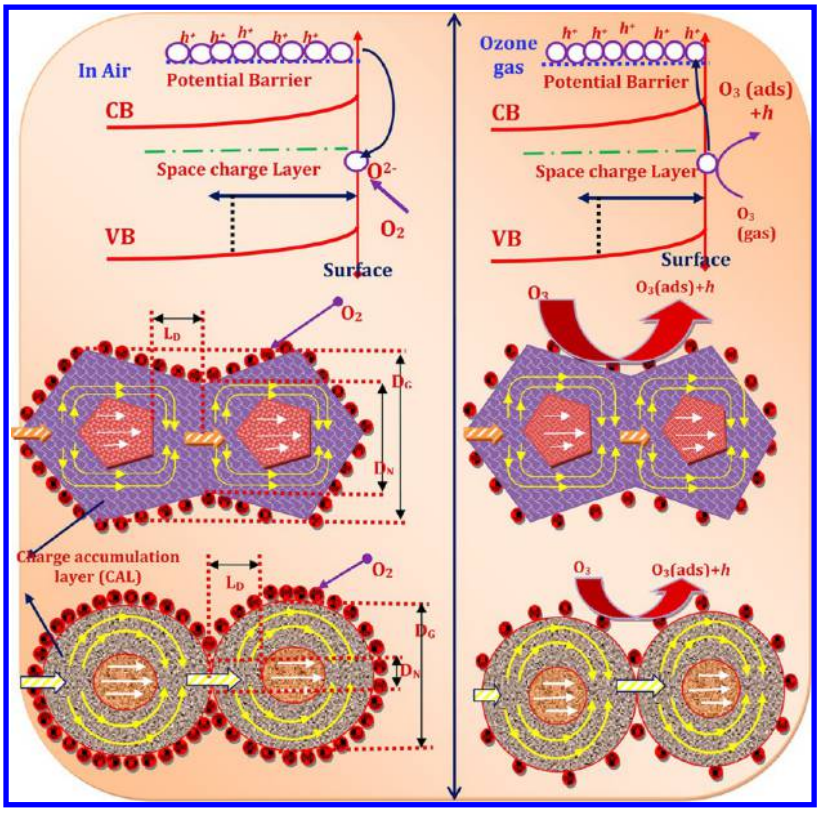

Figure 8. Energy band representation of the surface processes associated with the reaction at ambient oxygen (left) and ozone gas (oxidation gas) (right) (LD, Debye length; D_N, size of neck; D_G, size of particle).

view or the phenomenon was found to be reasonable based on a conducting model which mainly focuses on the active sensing layer (Debye layer) resistance and the grain-to-grain contact resistance, both of which are gas sensitive.[51]

In Figure 8 the schematic representation of the surface layer and the corresponding energy band structure are presented. We can observe that the flower structure constituted of $CuAlO_2$ nanoparticles (pentagon shape) has a larger grain size (D_G) compared to the hexagonal structure constituted of $CuAlO_2$ nanoparticles (oval shape), and thus, better gas-sensing sensitivity was obtained, as confirmed in Figure 6. Regarding the size factor, the larger the particle size, the smaller the effective contact surface per unit volume. This result also indicates that particles with relatively smaller size are more advantageous for ozone sensing. In addition, particles possessing not only comparable size but also diverse morphology will display strikingly effective contact surfaces.[52] The response of p-type $CuAlO_2$ materials is based on the change of the number of electrons in the conduction band after ozone gas interaction and its measurable effect on the resistance (decrease) of the semiconductor. The surface is where the crystal periodicity is interrupted, and this enables localized energy levels in the forbidden gap region. The energy levels available on the surface are called surface states, which capture electrons of ozone gas.[52] Conduction band or acceptor level holes prefer to flow to the high-energy surface states residing in the band gap. The acceptor holes move to the surface and take part in adsorbing oxygen onto the surface (Figure 8). This process forms a space charge region where positively charged donor atoms are on one side and negatively charged surface states on the other. The potential barrier formed on the surface due to the space-charge region and the height and depth of the bending depend on the surface charge. The Debye length (LD) is another parameter that affects the thickness of the depletion region (eq 3). L_D is a measure of the electrostatic screening in materials. It depends on the dielectric permittivity (ε), Boltzmann constant (K_B), temperature (T), electron charge (e), and carrier concentration (n_d).[53]

$$L_D = \sqrt{\frac{\varepsilon_0 \varepsilon k_B T}{e^2 n_d}} \tag{3}$$

The mechanism was reasonable based on a conduction model, which mainly focuses on the active sensing layer resistance and the grain-to-grain contact resistance, both of which are sensitive for gas detection in these materials based on reactions that change the concentration of adsorbed oxygen on the materials surface. Gas sensing response increases with decrease in grain size (D_G), increased neck diameter (D_N), and grain to grain contact, as suggesting by Lee and others.[47] In the present case, $CuAlO_2$ flower nanostructures have a larger grain size, face to face grain contact, and small neck diameter (D_N) when compared to $CuAlO_2$ hexagonal nanostructures. The hexagon with rough surface has smaller particles which are interconnected. This nature of the hexagonal nanostructure provides highly exposed surfaces and more pathways for electron exchange during gas diffusion/molecule capture and surface reaction, which makes the point to point grain contact surface area effective and increase in the amount of ozone gas adsorbed onto the surface.

4. CONCLUSIONS

In summary, we have developed unique flowers and hexagonal morphologies of $CuAlO_2$ constituted of nanoparticles with an

average size ~80 and 40 nm with good specific surface area, 59.8 and 70.8 m^2 g^{-1}, prepared by a facile and economical hydrothermal method. Through the experiment, it was observed that the surfactant (citric acid and CTAB) and operating parameters induced the Ostwald ripening mechanism, which has strong effects on the growth of different morphologies. In addition, it is revealed that the exposed surface of the $CuAlO_2$ functions as the reactive sites, owing to strong chemical bonds with the ozone gas molecules. The hexagonal $CuAlO_2$ based sensor showed excellent ozone gas response compared to $CuAlO_2$ flowers. Explanations for this behavior were proposed; the main sources for the improved performance of the sensor were identified as the control over morphology, particle size, and grain-to-grain contact. Furthermore, the sensor showed a nearly linear response to ozone concentration in the range 200−1150 ppb. Good response and recovery time indicated that the $CuAlO_2$ nanostructures with excellent surface active sites are a promising candidate for enhanced performance ozone gas sensors at ppb-level. These $CuAlO_2$ nanostructures are also expected to be useful for other potential applications, such as dye-sensitized solar cells, biosensors, and photocatalysts.

■ ASSOCIATED CONTENT

Supporting Information

SEM images, EDAX analyses, and XRD of $CuAlO_2$ samples. This material is available free of charge via the Internet at http://pubs.acs.org.

■ AUTHOR INFORMATION

Corresponding Authors

*Phone: +55 (16) 33739828. Fax: +55 (16) 33739824. E-mail address: sthirumalairajan@gmail.com.

*Phone: +55 (16) 33739828. Fax: +55 (16) 33739824. E-mail address: valmor@ifsc.usp.br.

Notes

The authors declare no competing financial interest.

■ ACKNOWLEDGMENTS

S.T. gratefully acknowledges Brazilian research financing institutions, CAPES, FAPESP/CEPID (2013/19049-0), and INCTMN/CNPq (10/20582-6), for carrying out this research, and Brazilian Nanotechnology National Laboratory (LNNano-CNPEM) for technical support during the X-ray photoelectron spectroscopy work.

■ REFERENCES

(1) Bai, S. L.; Zhang, K. W.; Luo, R. X.; Li, D. Q.; Chen, A. F.; Liu, C. C. Low-Temperature Hydrothermal Synthesis of WO_3 Nanorods and their Sensing Properties for NO_2. *J. Mater. Chem.* **2012**, *22*, 12643−12650.

(2) Ji, X. B.; Lu, W. C.; Ma, H. P. Shape-Controlled Synthesis of Porous Screw-Cap-like Indium Tin Oxide and its Application for Gas Sensing. *CrystEngComm* **2012**, *14*, 7145−7148.

(3) Barsan, N.; Simion, C.; Heine, T.; Pokhrel, S.; Weimar, U. Modeling of Sensing and Transduction for P-Type Semiconducting Metal Oxide Based Gas Sensors. *J. Electroceram.* **2010**, *25*, 11−19.

(4) Zhang, G.; Dang, L.; Wang, R.; Fu, H.; Shi, K. Design and Construction of CO_3O_4/PEI−CNTs Composite Exhibiting Fast Responding CO Sensor at Room Temperature. *CrystEngComm* **2013**, *15*, 4730−4738.

(5) Thirumalairjan, S.; Girija, K.; Mastealro, V. R.; Ponpandian, N. Surface Morphology-Dependent Room-Temperature $LaFeO_3$ Nanostructure Thin Films as Selective NO_2 Gas Sensor Prepared by Radio Frequency Magnetron Sputtering. *ACS Appl. Mater. Interfaces* **2014**, *6*, 13917−13927.

(6) Renard, L.; Brötz, J.; Fuess, H.; Gurlo, A.; Riedel, R.; Toupance, T. Hybrid Organotin and Tin Oxide-based Thin Films Processed from Alkynylorganotins: Synthesis, Characterization, and Gas Sensing Properties. *ACS Appl. Mater. Interfaces* **2014**, *6*, 17093−1710.

(7) Renard, L.; Elhamzaoui, H.; Jousseaume, B.; Toupance, T.; Laurent, G.; Ribot, F.; Saadaoui, H.; Brötz, J.; Fuess, H.; Riedeld, R.; Gurlo, A. Low-temperature H_2 Sensing in Self-assembled Organotin Thin Films. *Chem. Commun.* **2011**, *47*, 1464−1466.

(8) Gurlo, A. Nanosensors: Towards Morphological Control of Gas Sensing Activity. SnO_2, In_2O_3, ZnO and WO_3 Case Studies. *Nanoscale* **2011**, *3*, 154−165.

(9) Air Quality Guidelines Global Update **2005**, World Health Organization, Regional Office for Europe, WHO Regional Publications, European Series; Copenhagen, 2006.

(10) Yang, M.; He, J.; Hu, X.; Yan, C.; Cheng, Z. CuO Nanostructures as Quartz Crystal Microbalance Sensing Layers for Detection of Trace Hydrogen Cyanide Gas. *Environ. Sci. Technol.* **2011**, *45*, 6088−6094.

(11) Li, J. Y.; Xiong, S. L.; Xi, B. J.; Li, X. G.; Qian, Y. T. Synthesis of CuO Perpendicularly Cross-Bedded Microstructure *via* A Precursor-Based Route. *Cryst. Growth Des.* **2009**, *9*, 4108−4115.

(12) Triche, E. W.; Gent, J. F.; Holford, T. R.; Belanger, K.; Bracken, M. B.; Becket, W. S.; Naeher, L.; Leaderer, B. P. Low-Level Ozone Exposure and Respiratory Symptoms in Infants. *Environ. Health Perspect.* **2006**, *114*, 911−916.

(13) Katsarakis, N.; Bender, M.; Cimalla, V.; Gagaoudakis, E.; Kiriakidis, G. Ozone Sensing Properties of DC-sputtered, c-axis Oriented ZnO Films at Room Temperature. *Sens. Actuators, B* **2003**, *96*, 76−81.

(14) Korotcenkov, G.; Blinov, I.; Ivanov, M.; Stetter, J. R. Ozone Sensors on the Base of SnO_2 Thin Films Deposited by Spray Pyrolysis. *Sens. Actuators, B* **2007**, *120*, 679−686.

(15) Aliwell, S. R.; Halsall, J. F.; Pratt, K. F. E.; Sullivan, J. O.; Jones, R. L.; Cox, R. A.; Utembe, S. R.; Hansford, G. M.; Williams, D. E. Ozone Sensors Based on WO_3: A Model for Sensor Drift and A Measurement Correction Method. *Meas. Sci. Technol.* **2001**, *12*, 684−690.

(16) Nakagawa, H.; Okazaki, S.; Asakura, S.; Shimizu, H.; Iwamoto, I. A New Ozone Sensor for an Ozone generator. *Sens. Actuators, B* **2001**, *77*, 543−547.

(17) Zheng, X. G.; Taniguchi, K.; Takahashi, A.; Liu, Y.; Xu, C. N. Room Temperature Sensing of Ozone by Transparent p-Type Semiconductor $CuAlO_2$. *Appl. Phys. Lett.* **2004**, *85*, 1728−1729.

(18) Zhou, S.; Fang, X.; Deng, Z.; Li, D.; Dong, W.; Tao, R.; Meng, G.; Wang, T. Room Temperature Ozone Sensing Properties of p-Type $CuCrO_2$ Nanocrystals. *Sens. Actuators, B* **2009**, *143*, 119−123.

(19) Valmor, R. M.; Sergio, C. Z.; Luis, F. S.; Pedro, I. P.; Maria, I. B.; Jacques, G.; Khalifa, A. Ozone Gas Sensor Based on Nanocrystalline SrTi1−xFexO_3 Thin Films. *Sens. Actuators, B* **2013**, *181*, 919−924.

(20) Smith, J.; Van Steenkiste, T.; Wang, X. G. Thermal Photocatalytic Generation of H_2 over $CuAlO_2$ Nanoparticle Catalysts in H_2O. *Phys. Rev. B: Condens. Matter Mater. Phys.* **2009**, *79*, 041403.

(21) Thu, T. V.; Thanh, P. D.; Suekuni, K.; Hai, N. H.; Mott, D.; Koyano, M.; Maenosono, S. Synthesis of Delafossite $CuAlO_2$ p-Type Semiconductor with a Nanoparticle-Based Cu(I) acetate-Loaded Boehmite Precursor. *Mater. Res. Bull.* **2011**, *46*, 1819−1827.

(22) Shahriari, D. Y.; Barnabe, A.; Mason, T.; Poeppelmeier, K. R. A High-Yield Hydrothermal Preparation of $CuAlO_2$. *Inorg. Chem.* **2001**, *40*, 5734−5735.

(23) David, O. S.; Graeme, W. W. Conductivity Limits in $CuAlO_2$ from Screened-Hybrid Density Functional Theory. *J. Phys. Chem. Lett.* **2010**, *1*, 3195−3199.

(24) Volanti, D. P.; Felix, A. A.; Orlandi, M. O.; Whitfield, G.; Yang, D. J.; Longo, E.; Tuller, H. L.; Varela, J. A. The Role of Hierarchical Morphologies in the Superior Gas Sensing Performance of CuO-Based Chemiresistors. *Adv. Funct. Mater.* **2013**, *23*, 1759−1766.

(25) Girija, K.; Thirumalairajan, S.; Patra, A. K.; Mangalaraj, D.; Ponpandian, N.; Viswanathan, C. Organic Additives Assisted Synthesis of Mesoporous β-Ga_2O_3 Nanostructures for Photocatalytic Dye Degradation. *Semicond. Sci. Technol.* **2013**, *28*, 035015 (11pp).
(26) Alenezi, M. R.; Henley, S. J.; Emerson, N. G.; Silva, S. R. From 1D and 2D ZnO Nanostructures to 3D Hierarchical Structures with Enhanced Gas Sensing Properties. *Nanoscale* **2014**, *6*, 235−247.
(27) Prabhakar, R.; Kwak, W. K.; Yu, Y. T. Solvothermal Synthesis of ZnO Nanostructures and Their Morphology-Dependent Gas-Sensing Properties. *ACS Appl. Mater. Interfaces* **2013**, *5*, 3026−3032.
(28) Li, Z.; Zhao, Q.; Fan, W.; Zhan, J. Porous SnO_2 Nanospheres as Sensitive Gas Sensors for Volatile Organic Compounds Detection. *Nanoscale* **2011**, *3*, 1646−1652.
(29) Dittrich, T.; Dloczik, L.; Guminskaya, T.; Lux Steiner, M.; Grigorieva, N.; Urban, I. Photovoltage Characterization of $CuAlO_2$ Crystallites. *Appl. Phys. Lett.* **2004**, *85*, 742−744.
(30) Banerjee, A. N.; Kundoo, S.; Chattopadhyay, K. K. Synthesis and Characterization of p-type Transparent Conducting $CuAlO_2$ Thin film by DC sputtering. *Thin Solid Films* **2003**, *440*, 5−10.
(31) Tsuboi, N.; Takahashi, Y.; Kobayashi, S.; Shimizu, H.; Kato, K.; Kaneko, F. Delafossite $CuAlO_2$ Films Prepared by Reactive Sputtering using Cu and Al targets. *J. Phys. Chem. Solids* **2003**, *64*, 1671−1674.
(32) Deng, Z.; Zhu; Tao, R.; Dong, W.; Fang, X. Synthesis of $CuAlO_2$ Ceramics using Sol-gel. *Mater. Lett.* **2007**, *61*, 686−689.
(33) Zhao, S.; Li, M.; Liu, X.; Han, G. Synthesis of $CuAlO_2$ Nanofibrous Mats by Electrospinning. *Mater. Chem. Phys.* **2009**, *116*, 615−618.
(34) Jarman, R. H.; Bafiaa, J.; Gebreslasse, T.; Ingram, B.; David Carter, J. Synthesis of the p-type Semiconducting Ternary oxide $CuAlO_2$ using the Pechini Method. *Mater. Res. Bull.* **2013**, *48*, 3916−3918.
(35) Zhong, L. S.; Hu, J. S.; Liang, H. P.; Cao, A. M.; Song, W. G.; Wan, L. J. Self-Assembled 3D Flowerlike Iron Oxide Nanostructures and their Application in Water Treatment. *Adv. Mater.* **2006**, *18*, 2426−2431.
(36) Li, X. A.; Zhang, B.; Ju, C. H.; Han, X. J.; Du, Y. C.; Xu, P. Morphology-Controlled Synthesis and Electromagnetic Properties of Porous Fe_3O_4 Nanostructures from Iron Alkoxide Precursors. *J. Phys. Chem. C* **2011**, *115*, 12350−12357.
(37) Thirumalairajan, S.; Girija, K.; Ganesh, V.; Mangalaraj, D.; Viswanathan, C.; Ponpandian, N. Novel Synthesis of $LaFeO_3$ Nanostructure Dendrites: A Systematic Investigation of Growth Mechanism, Properties, and Biosensing for Highly Selective Determination of Neurotransmitter Compounds. *Cryst. Growth Des.* **2013**, *13*, 291−302.
(38) Hiroshi, Y.; Shin-ichiro, I.; Kazushige, U.; Hiroshi, K.; Hideo, H.; Noriaki, H. Electronic Structure and Optoelectronic Properties of Transparent p-Type conducting $CuAlO_2$. *J. Appl. Phys.* **2000**, *88*, 4159.
(39) Girija, K.; Thirumalairajan, S.; Patra, A. K.; Mangalaraj, D.; Ponpandian, N.; Viswanathan, C. Enhanced Photocatalytic Performance of Novel Self-assembled Floral β-Ga_2O_3 Nanorods. *Curr. Appl. Phys.* **2013**, *13*, 652−658.
(40) Ahmed, J.; Blakely, C. K.; Prakash, J.; Yu, M.; Wu, Y.; Poltavets, V. V. Scalable Synthesis of Delafossite $CuAlO_2$ Nanoparticles for p-type Dye-sensitized Solar Cells Applications. *J. Alloys Compd.* **2014**, *591*, 275−279.
(41) Ishiguro, T.; Ishizawa, N.; Mizutani, N.; Kato, M. High Temperature Structural Investigation of the Delafossite Type Compound $CuAlO_2$. *J. Solid State Chem.* **1982**, *41*, 132−137.
(42) Manoj, K. S.; Dussan, S.; Sharma, G. L.; Ram, S. K. Raman Scattering Measurements of Phonon Anharmonicity in $CuAlO_2$ Thin Films. *J. Appl. Phys.* **2008**, *104*, 113503.
(43) Hao, G.; Yue, W.; Yi, L. Nanocrystalline p-Type Transparent Cu−Al−O Semiconductor Prepared by Chemical-Vapor Deposition with $Cu(acac)_2$ and $Al(acac)_3$ Precursors. *Appl. Phys. Lett.* **2000**, *76*, 3959.
(44) Santra, S.; Das, N. S.; Chattopadhyay, K. K. Sol-gel Synthesis and Characterization of Wide Band Gap p-Type Nanocrystalline $CuBO_2$. *Mater. Lett.* **2013**, *92*, 198−201.
(45) Ghosh, C. K.; Popuri, S. R.; Mahesh, T. U.; Chattopadhyay, K. K. Preparation of Nanocrystalline $CuAlO_2$ through Sol−gel Route. *J. Sol-Gel Sci. Technol.* **2009**, *52*, 75−81.
(46) Sakai, G.; Matsunaga, N.; Shimanoe, K.; Yamazoe, N. Theory of Gas-Diffusion Controlled Sensitivity for Thin Film Semiconductor Gas Sensor. *Sens. Actuators, B* **2001**, *80*, 125−131.
(47) Kim, H. J.; Lee, J. H. Highly Sensitive and Selective Gas Sensors using p-type Oxide Semiconductors: Overview. *Sens. Actuators, B* **2014**, *192*, 607−627.
(48) Zhang, Y.; Xu, J. Q.; Xiang, Q.; Li, H.; Pan, Q. Y.; Xu, P. C. Brush-Like Hierarchical ZnO Nanostructures: Synthesis, Photoluminescence and Gas Sensor Properties. *J. Phys. Chem. C* **2009**, *113*, 3430−3435.
(49) Hansen, B. J.; Kouklin, N.; Lu, G.; Lin, I. K.; Chen, J.; Zhang, X. Transport, Analyte Detection, and Opto-Electronic Response of p-Type CuO Nanowires. *J. Phys. Chem. C* **2010**, *114*, 2440−2447.
(50) Yang, M.; He, J.; Hu, X.; Yan, C.; Cheng, Z. CuO Nanostructures as Quartz Crystal Microbalance Sensing Layers for Detection of Trace Hydrogen Cyanide Gas. *Environ. Sci. Technol.* **2011**, *45*, 6088−6094.
(51) Kuo, C. H.; Chen, C. H.; Huang, M. H. Seed-Mediated Synthesis of Monodispersed Cu_2O Nanocubes with Five Different Size Ranges from 40 to 420 nm. *Adv. Funct. Mater.* **2007**, *17*, 3773−3780.
(52) Ingram, B. J.; Mason, T. O.; Asahi, R.; Park, K. T.; Freeman, A. J. Electronic Structure and Small Polaron Hole Transport of Copper Aluminate. *Phys. Rev. B: Condens. Matter Mater. Phys.* **2001**, *64*, 155114.
(53) Yoon, J. W.; Choi, J. K.; Lee, J. H. Design of a Highly Sensitive and Selective C_2H_5OH Sensor using p-Type Co_3O_4 Nanofibers. *Sens. Actuators, B* **2012**, *161*, 570−577.